26.8-m THz wireless transmission of probabilistic shaping 16-QAM-OFDM signals

(F) (SCI)

Shiwei Wang, Zijie Lu, Wei Li, et al.

COLLECTIONS

(F) This paper was selected as Featured

(SCI) This paper was selected as Scilight

View Online Export Citation CrossMark

ARTICLES YOU MAY BE INTERESTED IN

A new system for high-speed terahertz wireless communication
Scilight **2020**, 211109 (2020); https://doi.org/10.1063/10.0001342

160 Gbit/s photonics wireless transmission in the 300–500 GHz band
APL Photonics **1**, 081301 (2016); https://doi.org/10.1063/1.4960136

Review of terahertz and subterahertz wireless communications
Journal of Applied Physics **107**, 111101 (2010); https://doi.org/10.1063/1.3386413

APL Photonics
2021 Future
Luminary Collection
READ NOW

26.8-m THz wireless transmission of probabilistic shaping 16-QAM-OFDM signals F SCI

View Online   Export Citation   CrossMark

Shiwei Wang,[1] Zijie Lu,[1] Wei Li,[1] Shi Jia,[2] Lu Zhang,[1,a] Mengyao Qiao,[1] Xiaodan Pang,[3] (iD) Nazar Idrees,[1] Muhammad Saqlain,[1] Xiang Gao,[1] Xiaoxiao Cao,[1] Changxing Lin,[4] Qiuyu Wu,[4] Xianmin Zhang,[1] and Xianbin Yu[1,a] (iD)

AFFILIATIONS

[1]College of Information Science and Electronic Engineering, Zhejiang University, Hangzhou 310027, China

[2]Department of Photonics Engineering, Technical University of Denmark, Kgs. Lyngby DK-2800, Denmark

[3]Kista High-Speed Transmission Lab, Royal Institute of Technology, SE-10044 Stockholm, Sweden

[4]Microsystem and Terahertz Research Center, Institute of Electronic Engineering, China Academy of Engineering Physics, Mian Yang 621900, China

[a]Authors to whom correspondence should be addressed: zhanglu1993@zju.edu.cn and xyu@zju.edu.cn

ABSTRACT

Recently, remarkable efforts have been made in developing wireless communication systems at ultrahigh data rates, with radio frequency (RF) carriers in the millimeter wave (30–300 GHz) and/or in the terahertz (THz, >300 GHz) bands. Converged technologies combining both the electronics and the photonics show great potential to provide feasible solutions with superior performance compared to conventional RF technologies. However, technical challenges remain to be overcome in order to support high data rates with considerably feasible wireless distances for practical applications, particularly in the THz region. In this work, we present an experimental demonstration of a single-channel THz radio-over-fiber (RoF) system operating at 350 GHz, achieving beyond 100 Gbit/s data rate over a 10-km fiber plus a >20-m wireless link, without using any THz amplifiers. This achievement is enabled by using an orthogonal frequency division multiplexing signal with a probabilistic-shaped 16-ary quadrature amplitude modulation format, a pair of highly directive Cassegrain antennas, and advanced digital signal processing techniques. This work pushes the THz RoF technology one step closer to ultrahigh-speed indoor wireless applications and serves as an essential segment of the converged fiber-wireless access networks in the beyond 5G era.

I. INTRODUCTION

With the rapid development of the Internet industry and the increasing number of wireless end users, the traffic demand for wireless service has been increasing dramatically. It is foreseen that the demand for wireless connection speed will go beyond 100 Gbit/s and even approach Tbit/s in the coming decades.[1] In order to fulfill the broad bandwidth requirements for future communication, much attention is paid to explore new frequency resources, such as mm-wave/THz wireless communications and optical wireless communications.[2] Among them, the THz band (0.3–10 THz) is a promising candidate, as it not only meets the bandwidth demand, but also is robust to, for instance, dust perturbation compared to

optical wireless communications technology.[3–5] Recently, considerable efforts have been therefore made in researching and developing THz wireless communication systems for the delivery of very high data rates.[6–15] Benefiting from the advantages of a large modulation bandwidth and small nonlinear effect, photonics-assisted THz communications have been developed rapidly, especially in terms of transmission rates.[6,7] For example, a net data rate of 260 Gbit/s THz photonic-wireless transmission was reported in the 0.4 THz band with a single pair of THz antennas,[8] which is among the highest reported data rates to date. However, although many THz wireless transmissions exceeding 100 Gbit/s have been reported, the demonstrated wireless distances are mostly within the range of 0.5 m.[8–10] The main factor limiting the transmission distance of high-speed

THz signals is the limited radiating power of opto-electronic THz sources, resulting in a limited signal-to-noise ratio (SNR) at the receiver. Therefore, extending the transmission distance is currently of great significance to promote the development of high-speed THz communications.

Recently, there are a number of proposals on extending the transmission distance of THz wireless systems. Among them, one approach is to use a THz frequency window with a relatively low atmospheric attenuation. The atmospheric attenuation of 0–1000 GHz electromagnetic waves is shown in Fig. 1. By using a THz frequency window with a relatively lower atmospheric attenuation, the loss of terahertz signal during propagation is reduced, which in turn increases the transmission distance—for example, 100 Gbit/s 2 m wireless transmission at 350 GHz[16] and 131 Gbit/s 10.7 m wireless transmission at 408 GHz.[17] Another method is to use the probabilistic shaping (PS) technique on transmitted signals. This technique improves the wireless reach by reducing the average transmission energy per bit.[18,19] With the assistance of the PS technique, Wang *et al.* reported a wireless transmission of 25.6 Gbit/s probabilistic-shaped 16-ary quadrature amplitude modulation format (PS-16-QAM) signals with a distance of 1.41 m in the 450 GHz band.[18] Additionally, a 2 × 2 multiple-input multiple-output (MIMO) transmission of 132 Gbit/s PS-64-QAM signal over 1.8 m in the 400 GHz band was also demonstrated.[19] The third approach to increase the transmission distance is to increase the power budget of THz links, which is naturally dependent on the support of THz devices, e.g., high-gain THz antennas and amplifiers. In Ref. 20 for instance, a 50 Gbit/s wireless transmission at 300 GHz over 100 m was achieved by using a pair of high-gain antennas of 54 dBi. Moreover, a wireless communication system with 100 Gbit/s quadrature phase shift keying (QPSK) signals over 110 m in the 300-GHz band has been realized by using a THz power amplifier and a THz low noise amplifier.[21] The implementations of these high-speed THz links are foreseen to enable instant access to extremely fast wireless services, such as ultrahigh-definition-video conferences, THz personal wireless area networks, and ultrafast wireless backhaul links.
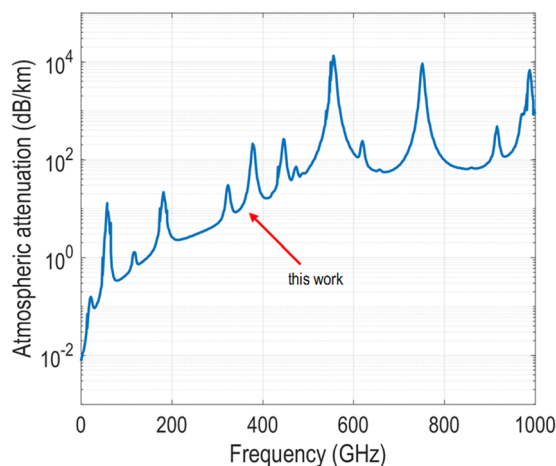
From a networking architecture point of view, it is important to efficiently deliver the data for high-speed wireless systems over the fiber-optic access network infrastructure, before reaching access points for end users. As we all know, the radio-over-fiber (RoF) technologies can be used to turn the antennas of traditional central stations into a distributed structure.[22] Figure 2 shows typical application scenarios of RoF systems. In the RoF systems, complex and high-cost equipment is installed in the central office to implement centralized signal processing, making the distributed access units simpler and stable at harsh environments. This arrangement effectively reduces the size of the access units and, thus, the installation and maintenance cost. Commonly, a photonic high-speed THz wireless communication RoF system can be seamlessly constructed on the existing fiber-optic networks, which share the city infrastructure and greatly reduce the cost for upgrading the network. In this sense, high-speed THz wireless communications is beneficial to exchange the constantly increasing capacity among base stations. In addition, the THz photonic wireless bridge is helpful to recover a communication channel and easy to establish when the optical backbone link is damaged in a disaster. Therefore, broadband high-speed THz photonic access communication systems have the potential to play an important role in developing next-generation networks. A THz communication system over a 2-km fiber and 5-cm wireless distance transmission with a data rate of 65 Gbit/s using a coherent radio-over-fiber approach was reported in Ref. 23, which still leaves room for further improvement to reach 100 Gbit/s.

In this paper, we propose and experimentally demonstrate a THz photonic wireless RoF communication system. To achieve high-speed THz transmission over extended wireless distances, the following efforts are made:

(1) The THz signal is photonically generated by optical mixing in a uni-traveling carrier photodiode (UTC-PD) and received by a Schottky diode-based sub-harmonic mixer for down-conversion. The THz carrier in the 350 GHz band is located in the low atmospheric attenuation frequency window.
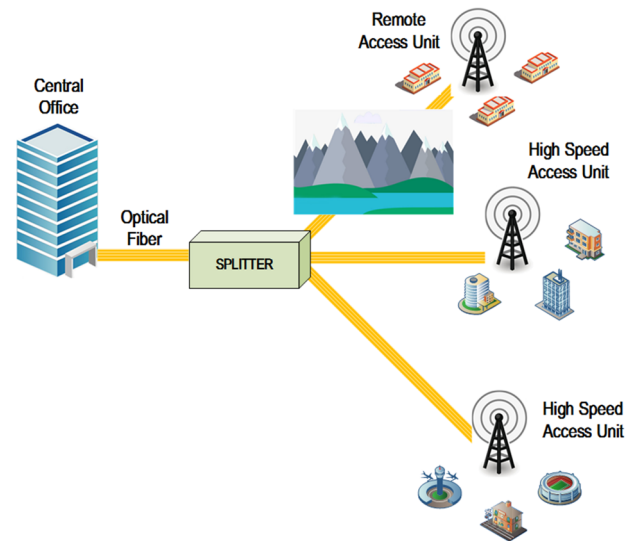

FIG. 1. Atmospheric attenuation of 0–1000 GHz electromagnetic waves.

FIG. 2. Structure and application scenarios of RoF systems.

(2) Orthogonal frequency division multiplexing (OFDM) technique is used as the modulation format to improve the system robustness against wireless channel impairments.

(3) The PS technique is applied on the OFDM signal to improve the system efficiency and reduce the bit-energy consumption.

(4) A pair of high-gain Cassegrain antennas is used for wirelessly transmitting and receiving THz signals.

The experimental results have successfully demonstrated a line rate of up to 106.2 Gbit/s transmission over 10-km single mode fiber (SMF) and 26.8-m wireless distance. It is noted that the line rate is calculated after removing the pilot and cyclic prefix (CP) overhead.

II. THz PHOTONIC LINK

A. Experimental setup

Figure 3 shows the schematic diagram of the proposed experiment. The whole setup consists of three sections emulating different parts of the network, namely, one central station, one base station, and one end user. Part A in Fig. 3 is the central station part that performs the baseband signal modulation. Part B is the base station part, which is connected to the central station through a piece of SMF of 10 km, and implements the photonic generation of THz signals based on photo-mixing, where a UTC-PD (NTT Electronics Corp. IOD-PMJ-13001) is used as the THz emitter operating in the frequency range of 280–380 GHz, with a maximum output power of −9.5 dBm at 350 GHz when the photocurrent reaches 7 mA.[24] Part C of the schematic illustrates the end-user part, where a Schottky mixer operating in the frequency band 325–500 GHz is used to receive

and down-convert THz signals into the intermediate frequency (IF) domain with a 40 GHz IF bandwidth at the reception side. The wireless transmission distance between the base station and the end user is 26.8 m.

In the experiment, we use two tunable external cavity lasers (ECLs, <100 kHz linewidth) as optical sources to emit C-band continuous-wave (CW) wavelengths. First, in the central station, the wavelength of ECL1 centered at 1550 nm is launched into a dual-parallel Mach–Zehnder modulator (DPMZM, Fujitsu FTM7962EP, 40 GHz bandwidth, 3.5 V half-wave voltage) with an output power of 15 dBm to implement the optical baseband modulation. The digital baseband data signal is generated by an arbitrary waveform generator (AWG, Keysight M8195A, 65 GSa/s sampling rate, 25 GHz analog bandwidth) and amplified by two electrical amplifiers (SHF 806E) with a 26 dB gain. The AWG is employed to map and modulate a pseudorandom bit sequence with a length of 2^{15}-1 bits sequence (PRBS-15) into a PS-16-QAM-OFDM signal at DPMZM and the electrical output amplitude is set as 80 mV. The inverse fast Fourier transformation (IFFT) point of OFDM is 1024, and the CP length is 16. The first two subcarriers are set to null. The subcarrier bandwidth and the CP length, which are used to reflect the channel bandwidth coherence property and time coherence property, respectively, are optimized to these values to obtain the best bit-error-rate (BER) performance based on the experimental data. In order to reduce the effect of peak to average power ratio (PAPR), the clipping method with a clipping ratio of 0.85 is used. Then the baseband signal is amplified by an Erbium-doped fiber amplifier (EDFA) and transmits through a piece of SMF of 10 km to the base station to implement an RoF transmission. In the base station, a roll of dispersion compensation fiber (DCF) with an overall dispersion of −164.3 ps/nm is used to compensate the
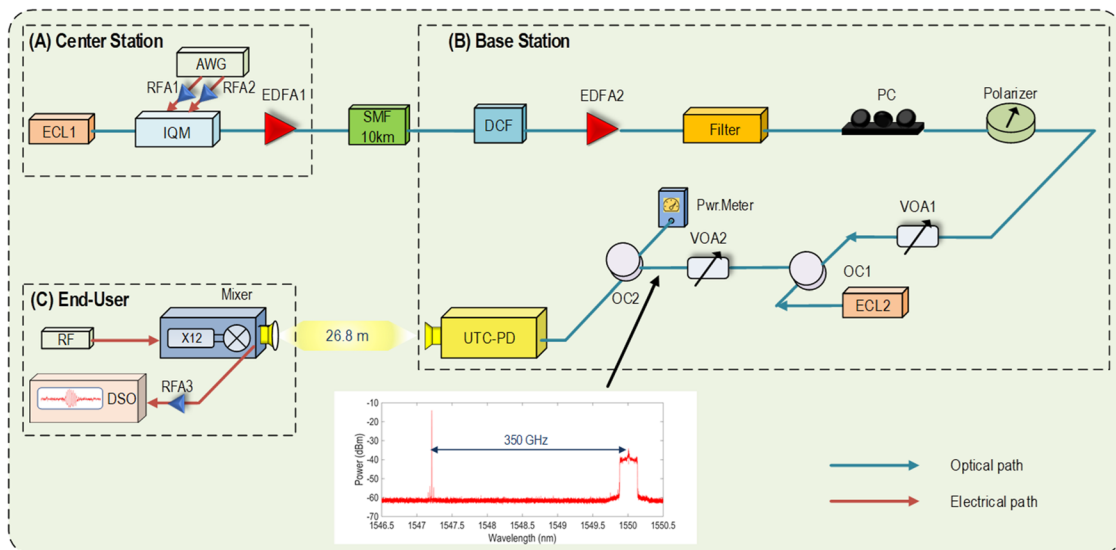

FIG. 3. Schematic experimental configuration for photonic high-speed THz wireless communication ROF system. ECL: external cavity laser, IQM: in-phase and quadrature modulator, AWG: arbitrary waveform generator, RFA: radio frequency amplifier, EDFA: Erbium-doped fiber amplifier, SMF: single mode fiber, DCF: dispersion compensation fiber, PC: polarization controller, VOA: variable optical attenuator, OC: optical coupler, UTC-PD: uni-traveling carrier photodiode, DSO: digital sampling oscilloscope, and RF: radio frequency generator. The inset: optical spectrum at the input of the UTC-PD.

chromatic dispersion induced by the SMF, in order to save the system overhead and increase the capacity. After amplification by the EDFA2, the signal is filtered by an optical band-pass filter to suppress the out-of-band amplified spontaneous emission (ASE) noise. As polarization was aligned by a polarizer controller (PC) and a polarizer, the baseband signal is power-balanced with the free-running local oscillator (LO) ECL2 by using a polarization maintaining variable optical attenuator (VOA1). The LO ECL2 is centered at 1547.2 nm with an output power of 15.3 dBm and combined with the baseband signal using a 3-dB optical coupler (OC1). Finally, the coupled signal is sent into the UTC-PD for photo-mixing and heterodyne generation of THz signals, with the power accurately controlled by a polarization maintaining VOA2 and monitored by a power meter. Moreover, the carrier frequency of the THz signal is determined by the wavelength difference between two lasers. The output of the UTC-PD is radiated into a 26.8 m free space line-of-sight (LOS) wireless link toward the receiver, as shown in Fig. 4. A pair of Cassegrain antennas with a 50 dBi gain is used for the THz wireless link. The THz wave is initially emitted from a horn with a physical aperture of 3.0×2.5 mm^2 and finally reflected into the free space by a parabolic reflector with a diameter of 160 mm. The inset illustrates the receiver side of the THz wireless transmission system. After mixing with a 12-order multiplied radio frequency (RF) signal from a vector signal generator (Keysight, E8267D), the THz signal is down-converted into the IF domain. The IF signal is then amplified by two cascaded radio frequency amplifiers (RFA) with a 40 dB gain, sampled and analog-to-digital converted by using a real-time broadband digital sampling oscilloscope (160 GSa/s, Keysight DSOZ594A, 59 GHz) for further digital signal processing.
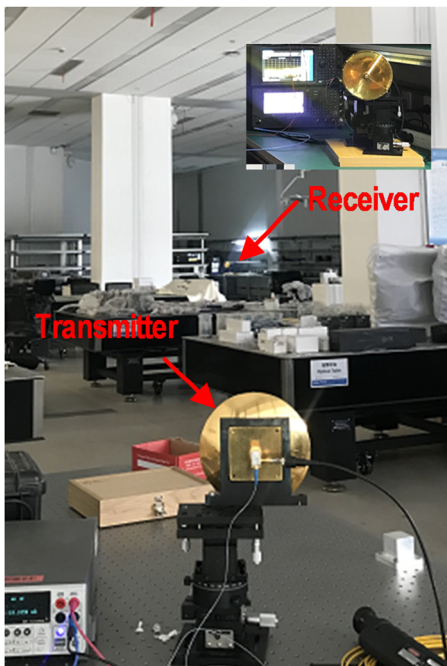
B. Digital signal processing (DSP) routine

The digital signal processing (DSP) routine at the transmitter side is shown in Fig. 5. A PS mapping module[25–27] is used to transform the PRBS sequence to PS-16-QAM symbols. In the PS scheme, each x-array and y-array of the 16-QAM constellations is distributed based on Maxwell–Boltzmann distribution, and the constellation points with lower energy (i.e., inner ring) are transmitted with a higher probability than the constellation points with higher energy (outer ring). As a result, the PS-16-QAM-OFDM has an improved noise tolerance and good bit-energy efficiency in the fiber channel and wireless channel, when power is insufficient. The probability mass function of the in-phase and quadrature-phase symbol of QAM is shown as follows:

$$P_X(x_i) = k \cdot e^{-v|x_i|^2}, \tag{1}$$

$$k = 1 / \sum_{j=1}^{M} e^{-v|x_i|^2}. \tag{2}$$

The symbol x_i means the discrete symbol of in-phase and quadrature-phase symbol of QAM, which corresponds to $\{-3, -1, +1, +3\}$ for the 16-QAM mapping. The variable v in the range of [0, 1] is used to control the shape of the probability distribution. A larger v will contribute to a larger variance of the probabilities at different symbols, which is adjusted in the experiment according to the channel SNR. The variable k is used to keep that the addition of all probabilities equals to 1. After subcarrier mapping, the IFFT module transforms the frequency domain symbols into the time domain
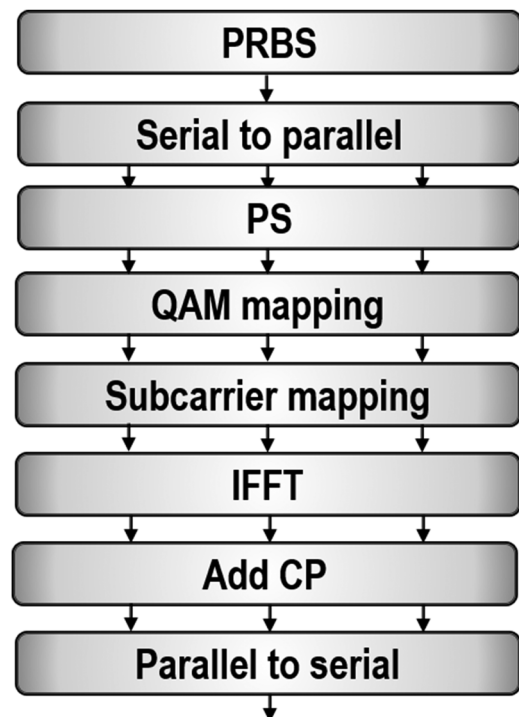

FIG. 4. The picture of actual THz wireless link.

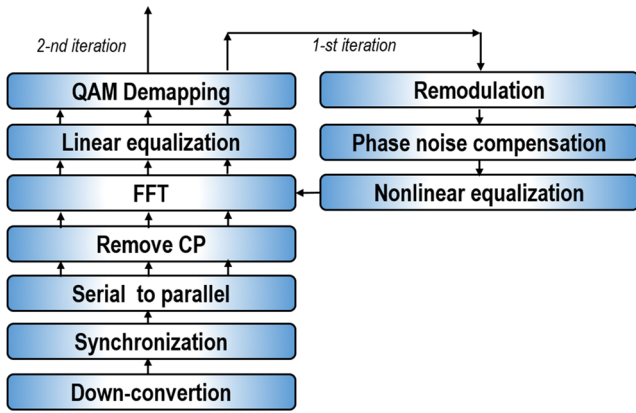FIG. 5. The DSP routine of the transmitter.

FIG. 6. The DSP routine of the receiver.

to realize OFDM modulation. Then, the CP with the same constellation size and distribution as PS-16-QAM symbols is inserted to reduce the influence of inter-symbol interference (ISI). To realize the synchronization of the PS-16-QAM-OFDM data frame, we add a pseudo-noise (PN) sequence with a length of 2^7-1 at the head of serial PS-16-QAM-OFDM data for synchronization.

The DSP routine at the receiver side is shown in Fig. 6. At the receiver, the signal is first captured from the scope, and then the signal is down-converted from the IF to the baseband. The autocorrelation of the PN sequence is used to find the frame head of the OFDM signal. After synchronization, the CP is first removed to mitigate the influence of multi-path interference induced ISI. Then, an FFT module transforms the time domain symbols into the frequency domain to realize OFDM demodulation. After that, equalization is used to recover the signal. The channel equalization is composed of linear equalization (LE), nonlinear equalization (NE), and phase noise compensation (PNC). First, the signal after the FFT module passes through the low-overhead lattice pilot based one-tap LE, which is used to compensate the system's linear response and to reduce the system's additive Gaussian noise influence.

Regarding the LE,[28] assuming G is the pilot interval, the lattice pilot positions at mth subcarrier correspond to symbol positions at $m\% G$, $m\% G + G$, $m\% G + 2G$, . . ., where % represents modulo calculation. We denote the transmitted pilot symbol before the IFFT at the mth subcarrier and nth OFDM symbol as $P_{m,n}$, and the received pilot symbol after the FFT at the mth subcarrier and nth OFDM symbol as $P'_{m,n}$. The channel response at the lattice pilot is first estimated by the least squares algorithm, as shown as follows:

$$H_{m,n} = P'_{m,n}/P_{m,n}\,_{|m=n\%G,n\%G+G,\dots}. \tag{3}$$

Then, the channel response of all subcarriers at the nth symbol is estimated by the interpolation of the pilot response with the symbol. The linear interpolation is used in this paper because of its low complexity,

$$H_{m,n|m=1,2,3,\dots} = \text{interp}(H_{m,n})_{|m=n\%G,n\%G+G,\dots}. \tag{4}$$

After interpolation operations of each symbol, the final response is obtained by averaging the response of all OFDM symbols

to reduce the influence originated from channel additive noise,

$$H_{m|m=1,2,3,\dots} = \sum_{n=1}^{N} H_{m,n}/N. \tag{5}$$

Since the lattice pilot symbols are interleaved in both the time and frequency domains, a better estimation of the linear response with a much smaller pilot overhead can be achieved. Finally, only 1% pilot overhead is needed for the experiment. After the LE, the signal is equalized with H_m. The frequency domain symbols after the LE are re-modulated to the time domain, and before generating a time domain symbol $\tilde{x}$, the phase noise and the frequency offset induced by two optical ECLs are mitigated by the spectrum estimation and PNC.[17]

After the PNC, the NE is performed based on the Volterra series nonlinear model in the time domain to estimate and equalize the nonlinear impairment. A truncation based Volterra series nonlinear model is used for estimating the nonlinearity components, which considers only the 2nd-order and the 3rd-order terms in this work. In the time domain, the transmission model is expressed as follows:

$$y(n) = w + \sum_{i=0}^{M_1-1} h_1(i)x(n-i) + \sum_{i=0}^{M_2-1}\sum_{j=i}^{M_2-1} h_2(i,j)x(n-i)x(n-j)$$

$$+ \sum_{i=0}^{M_3-1}\sum_{j=i}^{M_3-1}\sum_{k=j}^{M_3-1} h_3(i,j,k)x(n-i)x(n-j)x(n-k) + \cdots, \tag{6}$$

where n is the index of time domain samples, $x(n)$ is the OFDM signal after the LE and PNC, w is the additive Gaussian noise originating from the device background noise and channel impairments, $h_K(\dots)$ $(K > 0)$ is the Kth-order Volterra kernel corresponding to the linear $(K = 1)$ or nonlinear $(K > 1)$ channel responses, and M_K is the memory length of Kth-order effect. In the Volterra series based nonlinear equalization model, the number of multiplications is $\sum_{k=1}^{K}(M_k)^k$, which yields a complexity in the order of $O(M_K{}^K)$. Since linear distortions (w and h_1) have been well compensated with a low complexity and low overhead LE in Eqs. (3)–(5), we only consider h_2 and h_3 in Eq. (6) for nonlinear compensation. The nonlinear kernels are estimated by a recursive least square (RLS) algorithm[29] using the training symbols $\tilde{x}$ and $y(n)$ as follows:

$$e(i) = y^i(n) - \tilde{x}^i(n)^T \tilde{h}^{i-1}(n), \tag{7}$$

$$k^i(n) = P^{i-1}(n)\tilde{x}^i(n)\{\lambda + \tilde{x}^i(n)^T P^{i-1}(n)\tilde{x}^i(n)\}^{-1}, \tag{8}$$

$$P^i = \lambda^{-1}\{P^{i-1}(n) - k^i(n)\tilde{x}^i(n)^T P^{i-1}(n)\}, \tag{9}$$

$$\tilde{h}^i(n) = \tilde{h}^{i-1}(n) + e^i(n)k^i(n). \tag{10}$$

In the ith iteration, the estimated $\tilde{h}(n)$ is updated by Eq. (10) with the error signal $e(i)$ in Eq. (7) and the gain vector k^i from Eqs. (8) and (9). In Eqs. (7)–(10), the index n denotes the nth subcarrier and λ is a predefined constant before initialization. $P(n)$ is the inverse correlation matrix of the input signal. After obtaining the nonlinear kernels with the RLS algorithm and training symbols, the signal with nonlinear distortions is equalized by

subtracting the nonlinear noise using Eq. (11) with the estimated channel response $\tilde{h}(n)$ and estimated OFDM signal $\tilde{x}$,

$$y'(n) = y(n) - \sum_{i=0}^{M_2-1} \sum_{j=i}^{M_2-1} \tilde{h}_2(i,j)\tilde{x}(n-i)\tilde{x}(n-j)$$
$$- \sum_{i=0}^{M_3-1} \sum_{j=i}^{M_3-1} \sum_{k=j}^{M_3-1} \tilde{h}_3(i,j,k)\tilde{x}(n-i)\tilde{x}(n-j)\tilde{x}(n-k). \quad (11)$$

After equalization with Eq. (9), $y'(n)$ is utilized as the input for the decision-feedback module for the next iteration until the loop comes to the predefined iteration loop number.

C. Link budget

The link budget of a THz wireless communication system, which is usually calculated by the Friis formula, can characterize the performance of the system[30]

$$P_{Rx} = P_{Tx} + G_{Tx} + G_{Rx} - L_{Free-space}, \quad (12)$$

where P_{Rx} is the received power, P_{Tx} is the transmitted power in dBm, G_{Tx} and G_{Rx} represent the gains at the transmitter and receiver sides in dBi, respectively, and $L_{Free-space}$ is the free space path loss (FSPL) in dB. In Eq. (12), the FSPL is expressed as

$$L_{Free-space} = 20\log\frac{4\pi df}{c}, \quad (13)$$

where f is the operating frequency, c represents the speed of light in vacuum and d is the wireless distance between the transmitter and the receiver. We can notice that when the operating frequency gets higher and the distance gets longer, the FSPL increases quadratically. In the experiment, a wireless distance of 26.8 m yielded an FSPL of about 111.4 dB.

Table I lists the detailed link parameters in our system. The output power of UTC-PD is estimated at about -13 dBm when the input optical power is 13 dBm at the operating frequency of 350 GHz. By choosing the operating frequency working at the appropriate THz frequency window, the atmospheric attenuation is estimated to be approximately 0.3 dB for a 26.8 m distance in the laboratory environment. Due to the very large FSPL, we use a pair of antennas with a gain of 50 dBi for the wireless transmission.

TABLE I. Wireless link parameters.

Parameter	Value
Operating frequency	350 GHz
Optical power	13 dBm
THz power	-13 dBm
Tx antenna gain	50 dBi
Wireless distance	26.8 m
Free space path loss	111.4 dB
Atmospheric attenuation	0.3 dB
Rx antenna gain	50 dBi
Receiver loss	17 dB

III. EXPERIMENTAL RESULTS AND DISCUSSIONS

In this experimental work, we implement two THz communication systems, namely, with and without the RoF transmission over 10 km fiber, with the line rates of 106.2 Gbit/s and 119.1 Gbit/s, respectively. We measure the bit-error-rate (BER) performance as a function of optical power into the UTC-PD and successfully achieve good performance in both configurations.

First, we implement the THz wireless communication system without the fiber. Compared with Fig. 3, the SMF, DCF, and EDFA2 are removed from the experimental block diagram. In this system, the electrical spectrum of digital baseband fed into the AWG is shown in Fig. 7(a). The number of subcarriers is 550, and the bandwidth of the subcarrier is 63.5 MHz, yielding a total bandwidth of 34.9 GHz. It should be noted that the CP length and the number and the bandwidth of subcarriers are optimized to obtain the best BER in the experiment. The PS technology is applied to the system with the average information amount of each symbol set as 3.5 bit/symbol for all subcarriers, which satisfies the Maxwell–Boltzmann distribution in the Gaussian white noise channel, as shown in Fig. 7(b). The total
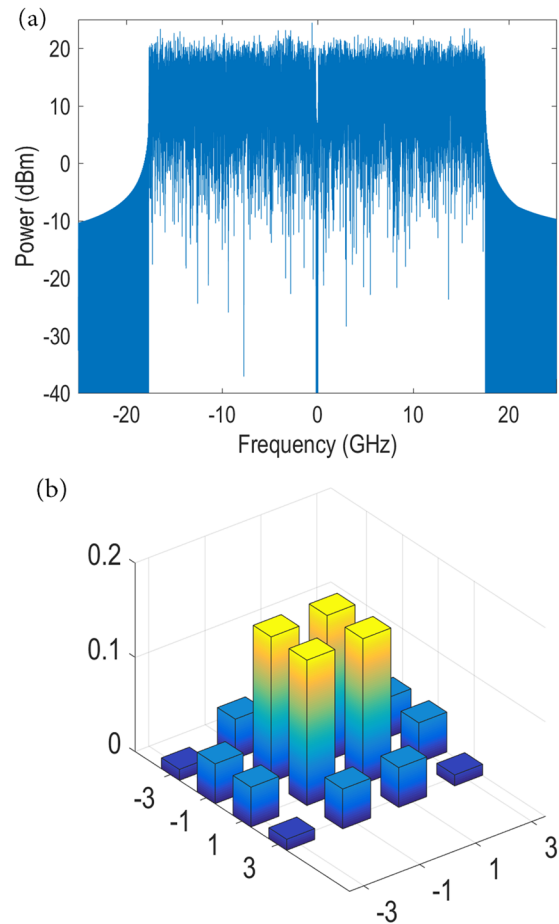

FIG. 7. (a) The FFT of the digital baseband signal generated by the AWG. (b) Probabilistic shaping 16-QAM signals with an average information amount each symbol of 3.5 bit/symbol.
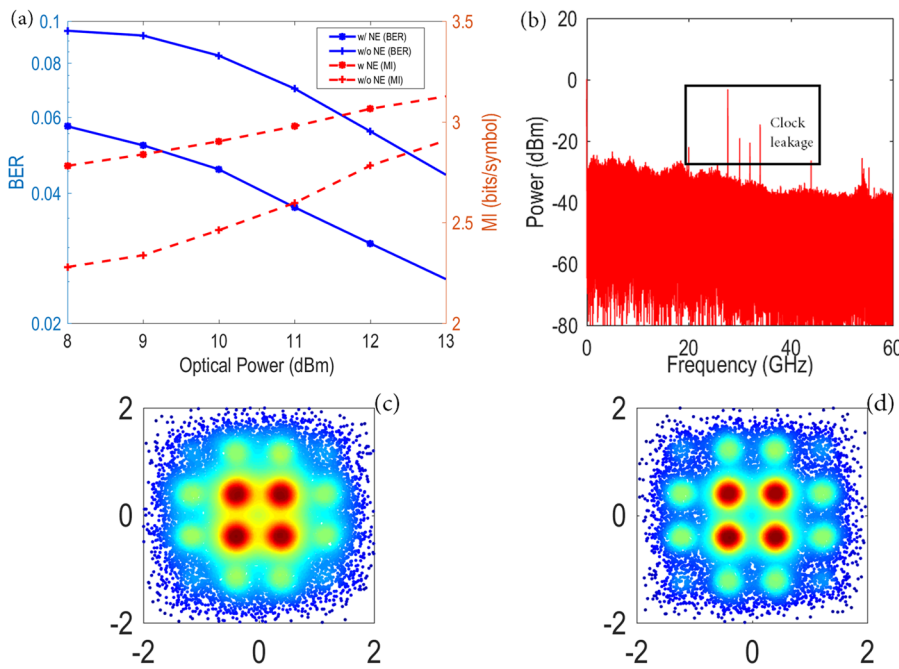
FIG. 8. (a) The measured BER and MI performance of THz signals without 10 km fiber transmission. (b) The electrical spectrum of PS-16-QAM-OFDM signals before down-conversion. (c) The constellation without the NE. (d) The constellation with the NE.

system overhead consists of three parts: pilot, PN, and CP. As the proportion of the PN in the signal is extremely low (around 0.1%), the overhead induced by the PN can be ignored. With reference to the line rate calculation for a single-carrier PS system,[31] the line rate of our multi-carrier PS-OFDM modulation scheme after taking into account the system overhead can be estimated as 3.5 × 34.9/(1% + 1%)/(1 + 16/1024) Gbit/s, reaching 119.1 Gbit/s. Here 1%, 16, and 1024 represent the pilot overhead, the CP length, and the number of IFFT points, respectively.

After 26.8 m wireless transmission, the signal is transmitted from the base station to the end user, and the corresponding BER and mutual information (MI) performance with and without the NE are displayed in Fig. 8(a). Here, the MI is calculated based on the input distribution P_X and channel transition probability $P_{Y|X}(Y|X)$, which is the probability of the received physical entity Y under the condition of a given transmitted physical entity X.[32] We can notice that as the optical power to the UTC-PD increases, both the BER and MI performance gets better on the one hand. On the other hand, the employment of the NE benefits to improve the BER and MI performance as well. We can notice from Fig. 8(a) that when the optical power is 13 dBm, the MI and BER reach 3.126 bits/symbol and 2.5×10^{-2}, respectively. In this experiment, the maximum line rate is 119.1 Gbit/s with a spectrum efficiency of 3.5 bit/symbol. For the illustration purpose, the received electrical spectrum before the DSP and the constellation after demodulation are presented in Figs. 8(b) and 8(c), which corresponds to the BER of 2.5×10^{-2}. We can notice that after a long distance wireless transmission, the signal at the receiver is weak with a poor SNR. In the electrical spectrum, the tones centered at 20 GHz and around 30–40 GHz are clock leakage induced by the oscilloscope.[33] It should be noted that the results are converged when the loop number is less than 3, which can be expected that the nonlinear equalizer will not introduce an additionally high latency.[29]
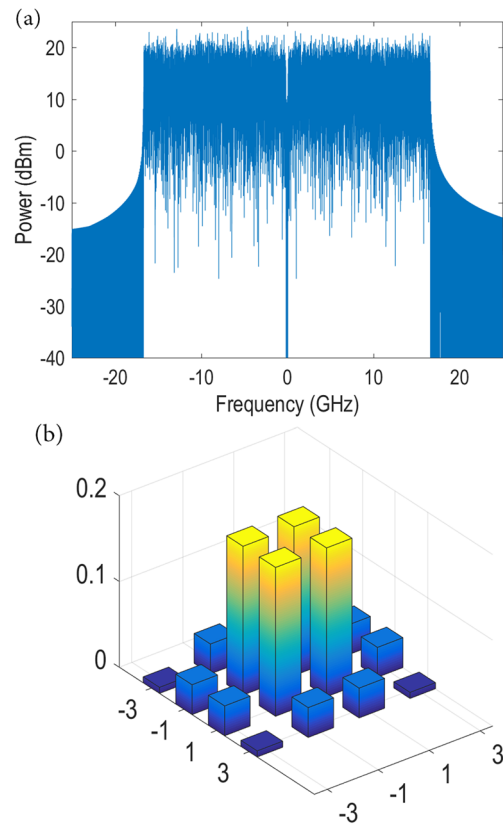

FIG. 9. (a) The FFT of the digital baseband signal generated by the AWG. (b) Probabilistic shaping 16-QAM signals with an average information amount each symbol of 3.3 bit/symbol.
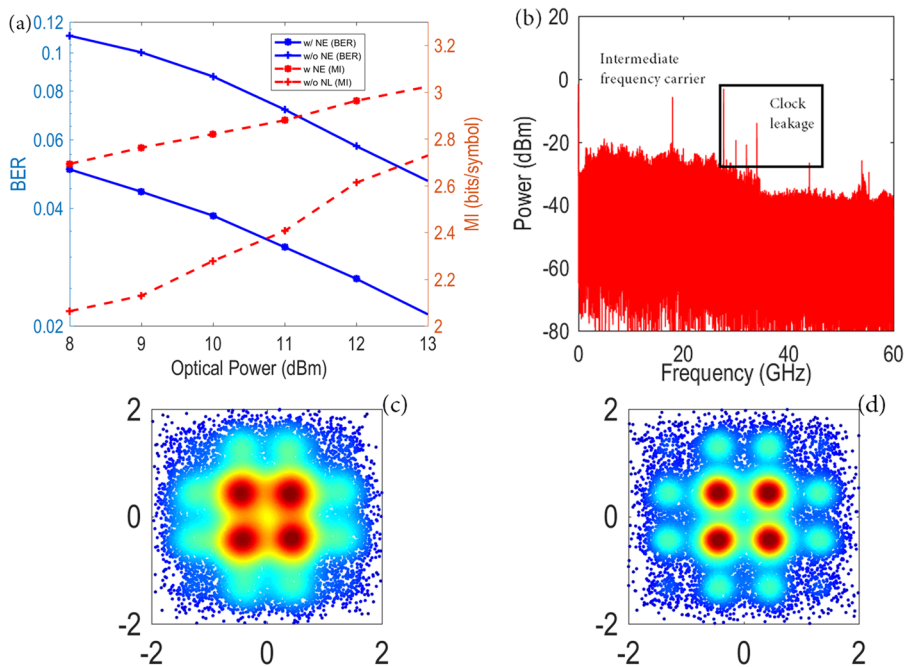
FIG. 10. (a) The measured BER and MI performance of THz signals with 10 km fiber transmission. (b) The electrical spectrum of PS-16-QAM-OFDM signals before down-conversion. (c) The constellation without the NE. (d) The constellation with the NE.

Then we experimentally demonstrate the PS-16-QAM-OFDM THz RoF wireless system with the configuration shown in Fig. 3. In this system, the electrical spectrum of the digital baseband signal fed into the AWG is shown in Fig. 9(a). The number of subcarriers is 520, and the bandwidth of the subcarrier is 63.5 MHz, yielding a total bandwidth of 33 GHz. Each subcarrier is modulated with the same PS-16-QAM-OFDM format. Here, the average information amount of each symbol is 3.3 bit/symbol, as shown in Fig. 9, and the line rate is $3.3 \times 33/(1\% + 1\%)/(1 + 16/1024)$ Gbit/s, reaching 106.2 Gbit/s. After the optical modulation in the DPMZM, the optical baseband signal is sent to the base station through an SMF of 10 km and coupled with the LO ECL. The coupled optical spectrum of two wavelengths with PS-16-QAM-OFDM signals is shown in the inset of Fig. 3.

After the wireless transmission, the signal is received at the end-user side. As shown in Fig. 10(a), we can notice that both the BER and MI exhibit better performance when the optical power to the UTC-PD increases. Benefited from the use of an NE, the BER and MI have been greatly improved, e.g., the BER drops to 2.1×10^{-2} and MI reaches 3.024 bits/symbol, when the optical power is 13 dBm. Here, we realize a line rate of up to 106.2 Gbit/s with a spectrum efficiency of 3.3 bit/symbol excluding the system overhead. For the illustration purpose, the received electrical spectrum before DSP and the constellation after demodulation are also presented in Figs. 10(b) and 10(c), which corresponds to the BER of 2.1×10^{-2}. The tone centered at 17.94 GHz in Fig. 10(b) is the intermediate frequency carrier after down-conversion. It is observed that the SNR in Fig. 10(b) is improved compared to that in Fig. 8(b), as a pre-amplifier (EDFA2) is additionally employed in the RoF system, for compensating the loss of fiber link and boosting the illumination to the UTC-PD. The PAPRs before and after the clipping process are around 10 dB and

8.7 dB, respectively. In order to investigate the transmission capacities in both cases, our systems are optimized by measuring the best BER performance. It is noted that the second EDFA is necessary for compensating the loss of fiber link, which introduces additional ASE noise. As a consequence, the line rate of fiber transmission system is reduced.

IV. CONCLUSION

We have experimentally implemented a high-speed THz photonic wireless communication system in the 350 GHz band based on RoF. In the experiment, wireless transmission of 16-QAM signals over a 26.8 m link is realized as the line rate reaches 119.1 Gbit/s. This enhancement is achieved by combining the PS, OFDM technology, high gain antennas, and advanced DSP routine. We combine the RoF link to build a quasi-realistic system for terahertz wireless transmission, achieving a wireless communication through a 10 km fiber transmission and 26.8 m wireless link with a line rate of 106.2 Gbit/s. This achievement pushes the THz RoF technology closer to ultrahigh-speed indoor wireless applications and is believed to serve as an essential segment of converged fiber-wireless access networks in the beyond 5 G era.

REFERENCES

[1] See https://www.cisco.com/c/en/us/solutions/collateral/service-provider/visual-networking-index-vni/white-paper-c11-741490.html for Cisco Visual Networking Index: Forecast and Trends, 2017–2022 White Paper.

[2] Z. Cao, X. Zhang, G. Osnabrugge, J. Li, I. M. Vellekoop, and A. M. Koonen, Light: Sci. Appl. **8**, 69 (2019).

[3] G. Fettweis, F. Guderian, and S. Krone, in *2011 IEEE Design, Automation and Test in Europe Conference* (IEEE, 2011), pp. 1–6.

[4] H.-J. Song and T. Nagatsuma, IEEE Trans. Terahertz Sci. Technol. **1**, 256 (2011).

[5] X. Yu, Y. Chen, M. Galili, T. Morioka, P. U. Jepsen, and L. K. Oxenloøwe, in *2014 International Conference on Transparent Optical Networks (ICTON)* (ICTON, 2014), pp. 1–4.

[6] A. J. Seeds, H. Shams, M. J. Fice, and C. C. Renaud, J. Lightwave Technol. **33**, 579 (2015).

[7] T. Nagatsuma, G. Ducournau, and C. C. Renaud, Nat. Photonics **10**, 371 (2016).

[8] X. Pang, S. Ji, O. Ozolins, X. Yu, H. Hu, L. Marcon, P. Guan, F. Da Ros, S. Popov, G. Jacobsen, M. Galili, T. Morioka, D. Zibar, and L. K. Oxenløwe, in *2016 IEEE Photonics Conference (IPC)* (IEEE, 2016), pp. 1–2.

[9] K. Takano, K. Katayama, S. Amakawa, T. Yoshida, and M. Fujishima, in *IEEE MTT-S International Microwave Symposium (IMS)* (IEEE, 2017), pp. 793–796.

[10] X. Yu, S. Jia, H. Hu, M. Galili, T. Morioka, P. U. Jepsen, and L. K. Oxenløwe, APL Photonics **1**, 081301 (2016).

[11] S. Jia, G. Jacobsen, M. Galili, T. Morioka, D. Zibar, L. K. Oxenlowe, X. Pang, O. Ozolins, X. Yu, H. Hu, J. Yu, P. Guan, F. Da Ros, and S. Popov, J. Lightwave Technol. **36**, 610 (2018).

[12] X. Yu, R. Asif, M. Piels, D. Zibar, M. Galili, T. Morioka, P. U. Jepsen, and L. K. Oxenlowe, IEEE Trans. Terahertz Sci. Technol. **6**, 765 (2016).

[13] J. Ma, N. J. Karl, S. Bretin, G. Ducournau, and D. M. Mittleman, Nat. Commun. **8**, 729 (2017).

[14] G. Ducournau, D. Bacquet, J.-F. Lampin, P. Szriftgiser, K. Engenhardt, E. Lecomte, R. Kassi, and M. Zaknoune, Electron. Lett. **51**, 915 (2015).

[15] S. Jia, X. Yu, H. Hu, J. Yu, T. Morioka, P. U. Jepsen, and L. K. Oxenløwe, in *European Conference on Optical Communication (ECOC)* (ECOC, 2016), pp. 506–508.

[16] K. Liu, S. Jia, S. Wang, X. Pang, W. Li, S. Zheng, H. Chi, X. Jin, X. Zhang, and X. Yu, IEEE Photonics Technol. Lett. **30**, 1064 (2018).

[17] S. Jia, M. C. Lo, L. Zhang, O. Ozolins, A. Udalcovs, D. Kong, X. Pang, X. Yu, S. Xiao, S. Popov, J. Chen, G. Carpintero, T. Morioka, H. Hu, and L. K. Oxenløwe, in *2019 Optical Fiber Communications Conference and Exposition (OFC)* (IEEE, 2019), pp. Th1C.2.

[18] K. Wang, X. Li, M. Kong, P. Gou, W. Zhou, and J. Yu, in *2018 Optical Fiber Communications Conference and Exposition (OFC)* (IEEE, 2018), pp. 1–3.

[19] X. Li, J. Yu, L. Zhao, W. Zhou, K. Wang, M. Kong, G. Chang, Y. Zhang, X. Pan, and X. Xin, in *2019 Optical Fiber Communications Conference and Exposition (OFC)* (IEEE, 2019), pp. M4F.4.

[20] T. Nagatsuma, K. Oogimoto, Y. Yasuda, Y. Fujita, Y. Inubushi, S. Hisatake, A. M. Agoues, and G. C. Lopez, in *International Conference on Infrared, Millimeter, and Terahertz Waves (IRMMW-THz)* (IEEE, 2016), pp. 1–2.

[21] T. Harter, C. Füllner, J. N. Kemal, S. Ummethala, M. Brosi, E. Bründermann, W. Freude, S. Randel, and C. Koos, in *European Conference on Optical Communication (ECOC)* (ECOC, 2018), pp. 1–3.

[22] H. A. Raweshidy and S. Komaki, *Radio Over Fiber Technologies for Mobile Communications Networks* (Artech House, 2002).

[23] M. F. Hermelo, P.-T. Shih, M. Steeg, A. Ng'oma, and A. Stöhr, Opt. Express **25**, 19360 (2017).

[24] T. Ishibashi, Y. Muramoto, T. Yoshimatsu, and H. Ito, IEEE J. Sel. Topics Quantum Electron. **20**, 79 (2014).

[25] B. Liu, X. Li, Y. Zhang, X. Xin, and J. Yu, APL Photonics **2**, 056104 (2017).

[26] T. Fehenberger, D. Lavery, R. Maher, A. Alvarado, P. Bayvel, and N. Hanik, IEEE Photonics Technol. Lett. **28**, 786 (2016).

[27] G. Bocherer, F. Steiner, and P. Schulte, IEEE Trans. Commun. **63**, 4651 (2015).

[28] L. Zhang, J. Chen, A. Udalcovs, H. Louchet, T. Dippon, M. Gruen, X. Pang, R. Schatz, U. Westergren, S. Popov, S. Xiao, and O. Ozolins, in *European Conference on Optical Communication (ECOC)* (ECOC, 2019).

[29] L. Zhang, X. Hong, X. Pang, O. Ozolins, A. Udalcovs, R. Schatz, C. Guo, J. Zhang, F. Nordwall, K. M. Engenhardt, U. Westergren, S. Popov, G. Jacobsen, S. Xiao, W. Hu, and J. Chen, Opt. Lett. **43**, 182 (2018).

[30] H. T. Friis, Proc. IRE **34**, 254 (1946).

[31] J. Cho, X. Chen, S. Chandrasekhar, and P. Winzer, Opt. Express **26**, 9784 (2018).

[32] J. Cho and P. J. Winzer, J. Lightwave Technol. **37**, 1590 (2019).

[33] M. Chen, L. Zhang, K. Bai, F. Li, G. Liu, H. Zhou, and Q. Chen, IEEE Photonics Technol. Lett. **31**, 1791 (2019).